White Rose Research Online

eprints@whiterose.ac.uk
https://eprints.whiterose.ac.uk
Universities of Leeds, Sheffield and York

Deposited via The University of Leeds.

White Rose Research Online URL for this paper:
https://eprints.whiterose.ac.uk/id/eprint/97843/

Version: Accepted Version

Article:
Vanacore, EA, Rost, S and Thorne, MS (2016) Ultralow-velocity zone geometries resolved by multi-dimensional waveform modeling. Geophysical Journal International, 206 (1). pp. 659-674. ISSN: 0956-540X

https://doi.org/10.1093/gji/ggw114

Reuse
Items deposited in White Rose Research Online are protected by copyright, with all rights reserved unless indicated otherwise. They may be downloaded and/or printed for private study, or other acts as permitted by national copyright laws. The publisher or other rights holders may allow further reproduction and re-use of the full text version. This is indicated by the licence information on the White Rose Research Online record for the item.

Takedown
If you consider content in White Rose Research Online to be in breach of UK law, please notify us by emailing eprints@whiterose.ac.uk including the URL of the record and the reason for the withdrawal request.

UNIVERSITY OF LEEDS
University of Sheffield
UNIVERSITY of York

Ultralow-velocity zone geometries resolved by multi-dimensional waveform modeling.

E.A. Vanacore[1, 2], S. Rost[1], M.S. Thorne[3]

Abstract

Ultra-low velocity zones (ULVZs) are thin patches of material with strongly reduced seismic wave speeds situated on top of the core-mantle boundary (CMB). A common phase used to detect ULVZs is SP_dKS (SKP_dS), an SKS wave with a short diffracted P leg along the CMB. Most previous efforts have examined ULVZ properties using 1D waveform modeling approaches. We present waveform modeling results using the 2.5D finite difference algorithm PSVaxi allowing us better insight into ULVZ structure and location. We characterize ULVZ waveforms based on ULVZ elastic properties, shape, and position along the SP_dKS raypath. In particular, we vary the ULVZ location (e.g. source or receiver side), ULVZ topographical profiles (e.g. boxcar, trapezoidal, or Gaussian) and ULVZ lateral scale along great circle path (2.5º, 5º, 10º). We observe several waveform effects absent in 1D ULVZ models and show evidence for waveform effects allowing the differentiation between source and receiver side ULVZs. Early inception of the SP_dKS/SKP_dS phase is difficult to detect for receiver-side ULVZs with maximum shifts in SKP_dS initiation of ~3º in epicentral distance, whereas source-side ULVZs produce maximum shifts of SP_dKS initiation of ~5º, allowing clear separation of source- versus receiver-side structure. We present a case study using data from up to 300 broadband stations in Turkey recorded between 2005 and 2010. We observe a previously undetected ULVZ in the southern Atlantic Ocean region centered near 45º S, 12.5ºW, with a lateral scale of ~3°, V_P reduction of 10%, V_S reduction of 30%, and density increase of 10% relative to PREM.

1. Introduction

Ultra-low velocity zones (ULVZs) are thin layers (typically less than 20 km high) located on top of the CMB characterized by significant S and P wave velocity decreases on the order of tens of percent. Several studies have also detected a strong density increase on the order of 10% in ULVZs [e.g. Garnero and Jeanloz, 2000; Rost et al., 2005; Idehara 2011]. ULVZs seem to be regional features of the lowermost mantle with many areas probed showing no evidence for ULVZ structure [see McNamara et al, 2010 for review]. Several studies note ΔV_P to ΔV_S ratios of 1:3 which has been interpreted as evidence for a partially molten origin [Williams and

38 Garnero, 1996; Berryman, 2000; Hier-Majumder, 2008] with evidence for internal
39 structure due to melting processes [Rost et al., 2006; Hier-Majumder, 2014].
40 Nonetheless, iron enrichment of (Mg,Fe)O might also lead to similar material
41 properties [Wicks et al., 2010; Bower et al., 2011] in addition to iron enrichment of
42 perovskite and post-perovskite [Mao et al., 2006]. Possible origins of iron
43 enrichment include core-mantle reaction products in the vicinity of the CMB [Knittle
44 and Jeanloz, 1991], subducted banded-iron formations [Dobson and Brodholt,
45 2005], and pockets of remnant ancient basal magma ocean [Labrosse et al., 2007].
46 ULVZs may mark areas where mantle flow collects dense material [Hernlund
47 and Jellinek, 2010; Bower et al., 2011; McNamara et al., 2010; Nomura et al., 2011].
48 Current geodynamic predictions indicate that ULVZs may preferentially align near
49 the edges of Large Low Shear Velocity Provinces (LLSVPs) [McNamara et al., 2010],
50 regions characterized by ~3% S-wave velocity reductions beneath the Pacific and
51 Africa [e.g., Garnero and McNamara, 2008; Lekic et al., 2012]. However, these
52 geodynamic predictions are based on compositionally derived ULVZs, whereas
53 recent efforts indicate that partially molten ULVZs are likely formed within the
54 interior of LLSVPs [Li et al., 2013]. ULVZs have been tenuously linked to hotspot
55 volcanism [Rost et al., 2005; Burke et al., 2008; Thorne et al., 2013a] and may play a
56 significant role in the formation of mantle plumes and possibly the formation of
57 large igneous provinces [e.g. Burke and Torsvik, 2004]. Because ULVZs may be a
58 controlling factor in the formation of large scale mantle and surface features,
59 determining the geographic location, geometry, and geophysical characteristics of

ULVZs are key to unlocking not only the cause of these structures but also the role ULVZs play in large scale mantle dynamics.

ULVZs have been identified seismically by a number of studies using probes such as ScP, ScS, PcP, SKS, and SP_dKS/SKP_dS phases (for an overview of recent ULVZ detections see McNamara et al., [2010]). Each of these probes has trade-offs between the different ULVZ parameters, most notably between P- and S-wave velocity reduction and thickness. The core reflected phases (e.g. ScP, PcP, ScS) typically have good vertical resolution while sampling regional CMB structure; the diffracted phases (S_{diff}, $PKKP_{diff}$, and SP_dKS) are able to sample large lateral CMB areas with less vertical resolution. These tradeoffs can be reduced by combining several probes sampling the same CMB location [Jensen et al., 2013].

In this study we concentrate on characterizing the interaction of the SKS-SP_dKS/SKP_dS system (in the following denoted as SP_dKS) with ULVZ structures. SP_dKS forms a post-cursor to SKS due to a short P-wave diffraction along the CMB when SKS reaches the critical P-wave ray-parameter at the CMB (See Figure 1). This system is particularly sensitive to CMB structure and allows sampling of large geographic areas [e.g. Garnero and Helmberger, 1995; Garnero and Helmberger, 1996; Garnero and Helmberger, 1998; Thorne and Garnero, 2004; McNamara et al., 2010]. Most previous efforts have resolved ULVZ properties through 1D waveform modeling of SP_dKS [Garnero and Helmberger, 1995; Thorne and Garnero, 2004; Sun et al, 2012] although recently 2D and 3D waveform propagation techniques have also been used [Helmberger et al, 1996; Ni et al, 2003; Rondenay et al., 2010; Thorne et al, 2007; Thorne et al., 2013a,b; Jensen et al., 2013, Brown et al., 2015].

These studies have found ULVZ related waveform effects that are not detectable in 1D modeling such as a precursory phase to SKS due to a top side ULVZ conversion [Thorne et al., 2013b], early inception of SP_dKS/SKP_dS [Rondenay et al., 2010], and a secondary diffraction from the top of the ULVZ structure [Ni et al., 2003]. However, the majority of previous 2D and 3D efforts concentrated on simple ULVZ models such as boxcar shaped ULVZs located at the inception point of SP_dKS or along the most sensitive portion of the diffracted path [Jensen et al., 2013, Thorne et al., 2013].

Recent geodynamic modeling shows that ULVZ morphology is dependent on viscosity, density and convective vigor forming ULVZs with different shapes including symmetrical or asymmetrical triangles (as seen in profile) or flat topped structures with steep sides [e.g. Tan et al., 2002; Bower et al., 2010; McNamara et al., 2010, Hier-Majumder and Revenaugh, 2010]. In this study we model more realistic ULVZ structures by expanding from simple boxcar models to include Gaussian shaped and flat-topped trapezoidal structures of varying length. We also examine an expanded set of ULVZ locations in order to cover variation in the interaction of the diffracted P-leg with the ULVZ. We use a large dataset of synthetic ULVZ waveforms to infer the properties of SP_dKS recorded at 300+ stations located in Turkey. We detect a small, roughly 3º wide, ULVZ located in the southern Atlantic Ocean in the vicinity of the African LLSVP. The improved modeling allows certainty of the location of the ULVZ on the receiver side, with northeastern and southwestern boundaries of the ULVZ being well defined.

2. Synthetic Modeling Methodology

We compute synthetic seismograms using the 2.5D rotationally symmetric, finite difference code PSVaxi, which uses a ring source with an amplitude that depends on the sine of the take-off angle to generate waveforms [Jahnke, 2009; Zhang et al, 2009; Thorne et al., 2013a,b]. We use a finite difference grid with 18433 grid points in the lateral (defined by co-latitude) direction and 4608 grid points in the depth direction that permits robust calculations of waveforms with frequencies up to ~0.5 Hz. With the chosen setup we are able to compute high frequency synthetics while keeping the memory and CPU time requirement manageable to simulate a large database of synthetic waveforms. We use a rotationally symmetric Earth model with a PREM background velocity model [Dziewonski and Anderson, 1981] and velocity variations representing ULVZ structure in the lowermost 50 km of the mantle. Synthetics are bandpass filtered between 0.04 Hz and 0.5 Hz for comparison with real data.

Here we use the PSVaxi method to simulate the effects of the location, size, and geometry of ULVZs on SP_dKS. To reduce the large parameter space (ULVZ location, thickness, seismic velocity,density, and ULVZ shape) we restrict modeling to P- and S-wave velocity reductions of -10% and -30% respectively and a density increase of +10% relative to PREM [Dziewonski and Anderson, 1981]. The height of the ULVZ above the CMB (h) is set to 10 km or 20 km to be in line with common ULVZ observations [e.g. Garnero and Vidale, 1999; Rost and Revenaugh, 2003]. The

general behavior of waveforms for 10 km thick ULVZs is the same for 20 km thick ULVZs, so we restrict our discussion to models with 10 km height for brevity. The source depth is set to 500 km with a location at 0º co-latitude and all structure is rotationally symmetric around a pole passing through the source and the center of the Earth. In the model setup, epicentral distance from the source is synonymous with co-latitude. This parameter space configuration reduces the variable space to the ULVZ shape, ULVZ length (W), and the location of the ULVZ (ϕ) in co-latitude (Figure 2).

We define three ULVZ shapes: (1) boxcar, (2) Gaussian, and (3) trapezoid, as shown in Figure 2. The boxcar model (Figure 2a) has previously been applied in 2D modeling [e.g. Rondenay et al., 2010; Thorne et al., 2013a, Thorne et al., 2013b] and is defined as an ULVZ with a length of W and an edge closest to the source (hereafter near edge) at ϕ_1 degrees co-latitude and a height (h) equal to 10 km as follows:

$$h(\phi) = h \quad \phi_1 \le \phi \le \phi_1 + W$$

Geodynamical modeling shows that a boxcar shaped ULVZ is not a realistic geometry. Instead, we expect ULVZs to form more pile-like structures dependent on the density and viscosity of the ULVZ and the ambient mantle [McNamara et al., 2010; Bower et al., 2011; Hier-Majumder and Revenaugh, 2010]. To simulate this more realistic ULVZ structure, we model a Gaussian shaped ULVZ and a flat topped trapezoidal ULVZ. The height of the Gaussian shaped ULVZ (Figure 2b) is defined as:

$$h_{ulvz}(\phi) = h\left(e^{-\left(\left(\phi_1 + \frac{W}{2}\right) - \phi\right)^2 \Big/ 2*\left(\frac{W}{2\pi}\right)^2} \right)$$

151

152

153 Here h_{ulvz} is defined by a function dependent on the co-latitude (ϕ) in degrees where
154 the maximum height of the ULVZ is h kilometers at the center point between the
155 near edge (ϕ_1) and the end of the anomaly at W degrees away from the near edge.
156 Note that 2π is an arbitrary factor to reduce the Gaussian function at the edges. The
157 trapezoidal shaped ULVZ model (Figure 2c) is defined by the piecewise function:

$$\left.\begin{array}{ll} h_{ulvz}(\phi) = h\left(e^{-\left(\left(\phi_1 + \frac{W}{4}\right) - \phi\right)^2 \Big/ \left(\frac{W}{2\pi}\right)^2} \right) & \phi_1 \le \phi \le \phi_1 + W/4 \\ h_{ulvz}(\phi) = h & \phi_1 + W/4 < \phi \le \phi_1 + 3W/4 \\ h_{ulvz}(\phi) = h\left(e^{-\left(\left(\phi_1 + \frac{3W}{4}\right) - \phi\right)^2 \Big/ \left(\frac{W}{2\pi}\right)^2} \right) & \phi_1 + 3W/4 < \phi \le \phi_1 + W \end{array}\right\}$$

158

159

160 The function defines a trapezoid with Gaussian tapered sides that are ¼ of the
161 anomaly length and a flat top with thickness h above the CMB for the remaining ½ of
162 the anomaly length. We do not explore more complex ULVZ geometries such as
163 asymmetric piles [e.g. McNamara et al., 2010; Rost et al., 2010; Cottar and
164 Romanowicz, 2012] in order to limit the model space.

165 We model ULVZs with three different lengths of 2.5º, 5º, and 10º (~150, 300,
166 and 600 km on the CMB respectively). The lateral extent of ULVZs is currently not

well-known, but the majority of studies indicate ULVZs are likely in this size range [e.g., McNamara et al., 2010]. We note however that larger ULVZ lateral dimensions are possible [e.g., Thorne et al., 2013; Cottaar and Romanowicz, 2012]. Because the SP_dKS waveforms are sensitive to the location of the ULVZ along the ray path [e.g., Rondenay et al., 2010, Thorne et al., 2013], for each model length and shape we also change the near edge location in 2.5º increments. We calculate waveforms for four base models, (1) the background PREM model [Dziewonski and Anderson, 1981], (2) a 1D ULVZ model, (3) a model with a boxcar ULVZ across the entire source-side region, and (4) a model with a boxcar ULVZ across the entire receiver side (Figure 4).

3. Synthetic modeling results

Our modeling reveals several waveform effects that have not been observed in previous studies. First, ULVZ presence leads to an early inception of SP_dKS with the magnitude of the shift dependent on the sidedness of the ULVZ. That is, the SP_dKS arrival is apparent at smaller epicentral distances than predicted by the PREM model. A similar effect was noted by Rondenay et al., [2010]. Here we extend these findings to show that the shift of the SP_dKS inception distance is larger for ULVZs occurring on the source side of the ray path than for receiver-side ULVZs (Table 1). Second, we describe an additional seismic phase $SPd_{top}KS$ and further internally reflected ULVZ multiples that are generated and interfere with the SP_dKS for finite sized ULVZs less than ~600 km wide (Figure 3). The strong waveform variations induced by these additional seismic phases might be interpreted as complicated ULVZ structure in 1D models. Third, the SP_dKS travel-time and

waveform anomalies are primarily sensitive to ULVZs where the P_{diff}-inception point is within or geographically near (within 10°) the ULVZ. Long P-diffractions before the interaction with the ULVZ structure lead to PREM-like waveforms. For finite ULVZs along a long diffraction path minor travel-time variations of SP_dKS are observable, but these variations are below the travel time resolution level of recorded data. In the following, we will discuss these results in more detail.

3.1. Source vs. Receiver Side ULVZs

A key difficulty in determining ULVZ position using SP_dKS waveforms is the inherent ambiguity between source- and receiver-side signals. 1D modeling methodologies produce identical results for source or receiver side signals and likely overpredict the amplitudes of ULVZ related phases [Thorne et al., 2013]. Consequently, studies exploiting this phase often assume ULVZ location based on other information such as crossing ray paths or additional information such as proximity to LLSVPs [e.g. Garnero and Helmberger, 1995; Garnero and Helmberger, 1996; Wen and Helmberger, 1998; Thorne and Garnero, 2004; Jensen et al., 2013]. Here we explore whether 2D modeling can be used to remove this ambiguity in source versus receiver side structure.

Most previous 1D and 2D waveform modeling studies have focused on 1D ULVZ layers or large boxcar shaped ULVZs [e.g. Ni et al. 2003; Rondenay et al. 2010]. Observations from these studies include: (1) early inception of SP_dKS relative to the inception of SP_dKS of non-ULVZ models (e.g. PREM), (2) change of the move out of ULVZ sampling SP_dKS compared to non-ULVZ SP_dKS, (3) a SKS precursor phase for SKS directly striking an ULVZ resulting in a S-to-P conversion at the entry point of

213 the ULVZ [Thorne et al., 2013b] (referred to as SPKS in Fig. 3), and (4) additional
214 SKS coda phases that can be categorized as diffractions along the top of the ULVZ (
215 $Sp_{top}PKS$ in Fig. 3). In this study we generate models for finite sized ULVZ models
216 that are either located at the SKS entrance/exit point at the CMB or sample the ULVZ
217 somewhere along the P-diffracted path of SP_dKS. We calculate synthetic traces for
218 epicentral distances of 90º to 130º (Figure 4). The expanded model space permits
219 clear detection of internally reflected ULVZ multiple phases (Figure 3). Full data
220 tables and waveform examples are included in the Supplementary material
221 (Supplementary Tables 1-9; Supplementary figures 1-36).
222 We establish our baseline by computing synthetic seismograms for the PREM
223 velocity model using PSVaxi (Figure 4a); three primary phases of interest, SKS,
224 SKS_{df}, and SP_dKS, are labeled. The SKS arrival time appears before zero because we
225 use a modified PREM model where we smooth the discontinuous jumps in seismic
226 velocity in the upper mantle. This is done to reduce the number of interfering
227 seismic arrivals in our wavefield. We plot waveforms aligned by the theoretical SKS
228 arrival time for an unmodified PREM model. All subsequent models discussed in this
229 manuscript are compared to this baseline calculation.
230 To explore the effects of 1D vs 2D models we initially run three models: (1) a 1D
231 ULVZ model (Figure 4b), (2) a source-sided ULVZ model (Figure 4c), and (3) a
232 receiver-sided ULVZ model (Figure 4d). The ULVZ models all consist of a 10km thick
233 ULVZ with a 10% drop in V_P, a 30% drop in V_S, and a 10% increase in density
234 relative to PREM. Note that waveforms and beyond 120º are dominated by the sPPP
235 phase labeled in (Figure 4a); SKS and SP_dKS waveform analysis beyond this distance

is therefore not considered. The 1-sided models (Figure 4c-d) produce identical waveforms with the expected SKS precursor and early inception of the SP_dKS phase in line with previous studies (e.g. Ni et al., 2003; Rondenay et al., 2010). This indicates that for very large ULVZs (>1000km) the sidedness of an ULVZ structure cannot be determined from the SP_dKS waveforms alone. However, the one-sided ULVZ model predictions differ from the 1D ULVZ model predictions in two distinct ways. First, the absolute time shift between the PREM predicted (blue line in Figure 4) SKS arrival and actual arrival is significantly greater (~1s) than the time shift predicted by the one-sided models. Second, the amplitudes of the ULVZ related phases, namely the SPKS precursor and SP_dKS/SKP_dS arrivals, are amplified in the 1D model by approximately 200% implying that 1D models in general overestimate the SP_dKS amplitude.

While it may not be possible to determine the location of the ULVZ at the source- or receiver-side of the ray path for large-scale ULVZ structures, our synthetic modeling indicates that it is possible to determine the ULVZ position for smaller scale ULVZs (i.e. for ULVZs less than ~600 km in length). Figure 5 shows synthetic waveforms for a 5º (300 km) wide ULVZ with its near edge located at 15º (source side) or 92.5º (receiver side) co-latitude for each of the 3 ULVZ shapes (boxcar, trapezoid, Gaussian). Since the SP_dKS raypath will encounter a source or receiver sided ULVZ in the same way (Figure 4), one would expect these waveforms to behave similarly for finite sized ULVZs, i.e. whether the ULVZ lies on the source- or receiver-side of the model would be irrelevant. However, the waveform behavior for the same model type is significantly different with respect to source- versus

receiver-side ULVZ locations (Figure 5). The source-side ULVZ models all contain a phase which first appears at an epicentral distance of ~97º with a ray parameter similar to the SP_dKS phase (<1s/º relative to $SKS_{ac,}$ indicated by the solid red line in Fig. 5a-c). This phase is not observed for ULVZs solely located on the receiver-side. This phase is also sensitive to the shape of the ULVZ. The largest amplitude arrivals are observed for the boxcar model, whereas this arrival is only weakly observed for the Gaussian models (Figure 5c). The trapezoid shaped models generate waveforms intermediary in amplitude between the Gaussian and boxcar models. This waveform behavior indicates that this phase is likely generated at the top of the ULVZ. Based on the traveltime and slowness of the phase one potential candidate is the ULVZ multiple phase $Ss_{top}PKS$ (blue line in Figure 3) where the phase reflects off the CMB the energy then reflects off the top of the ULVZ before propagating the remainder of the path similar to the SKS phase. This secondary phase (solid red line in Figure 5) interferes with the diffracted signal related to the top of the ULVZ, the SsP_dKS phase identified by Rondenay et al. [2010] (red dashed line in Figure 5); the two phases denoted by the red lines in Figure 6 destructively interfere to the point of eliminating all signal between 116º-118º epicentral distance. The interference is best observed in the boxcar models. This implies that if data are limited to this narrow band of distances the secondary phases are no longer useful for ULVZ identification.

The receiver-side ULVZ models do not contain $Ss_{top}PKS$ but do contain an additional arrival not present in the source-side ULVZ models. The additional arrival for receiver-side ULVZ models behaves similar to a point diffraction with a ray

parameter much greater than SP_dKS. The origin of this phase can be related to phases internally reflected within the ULVZ. The full waveform is produced by the interaction of the SKS with the ULVZ, which is quite different on the source and receiver side due to the ray path geometry; on the receiver side direct interaction between the SKS wavefield and the ULVZ is limited to rays spanning only a few degrees epicentral distance (Figure 6). On the source-side the SKS core-entry points are closely packed together leading to a waveform behavior closer to that expected from a 1D ULVZ model whereas the SKS exit points sample a significantly larger amount of area along the CMB and only a small distance range is influenced by small-scale ULVZs (Figure 4). This stretching of the wavefront at the receiver side might lead to the effect that the small-scale ULVZ acts as a point scatterer. The behavior of the secondary phases demarked by the red line in Figure 5(c-e) for receiver side ULVZ synthetics in combination with the fact that these phases have not been observed in recorded data may indicate that the point scatterer behavior occurs but is masked in real data by 3D wavefront healing effects. It is important to note that the SP_dKS arrivals alone are essentially identical for the source- and receiver-side structure; this implies that identification of the additional phases discussed above may provide a diagnostic tool for determining the location of ULVZ structures.

These SKS coda phases (solid red line in Figure 6) are pervasive in the entire model set tested in this study. Yet, these phases have not been identified in any study to date. The elusiveness of these phases can likely be attributed to several factors. Within the epicentral distances of interest (105º-120º), these codas phases

occur significantly later in time (between 5 and 20 s after the SKS arrival). Thus, these coda phases are likely outside the time window of interest traditionally used to study SP_dKS waveforms. When the coda phase is developing for ULVZs close to the theoretical inception point of SP_dKS it can either mimic SP_dKS (source side) or interfere with the observable SP_dKS phase (source and receiver side) (Figure 6 and Supplementary Figures). The possibility for future detection of these coda phases and their analysis to resolve the source-receiver side ambiguity for ULVZs lies with very large aperture arrays such as USArray allowing dense sampling of the CMB exit points or an "array of arrays" approach using multiple dense medium aperture arrays that may be capable of producing large epicentral distance sampling along similar backazimuths essentially reproducing the synthetic source-receiver geometry of the synthetic data.

3.2. SKS precursors

ULVZs generate precursory energy stemming from an S to P conversion as the wavefield enters the ULVZ, with a phase nomenclature of SPKS/SKPS for source/receiver side conversion points (e.g. Ni et al., 2003; Rondenay et al., 2010; Thorne et al., 2013). This phase is particularly important in resolving ULVZ location as the down-going (up-going for receiver-side ULVZ) S-leg of the SP_dKS raypath must intersect the ULVZ to generate this phase. For a 1D ULVZ model with a ULVZ thickness of 10 km this precursor is observed across all sampled epicentral distances (Figure 4). However, for finite length ULVZs the shape of the ULVZ determines the waveform behavior of the precursor (Figure 6, also see Supplemental Figures 1-36). Synthetics from this study indicate that ULVZs with a

length less than 2.5º (~150 km) do not produce a detectable precursor phase regardless of the ULVZ shape (Table 1 and Supplementary Figures 1-36). Moderate sized ULVZs with a length of 5º (~300 km) or 10º (~600km) are capable of producing the precursory phase, but are more detectable for flat topped structures, likely due to defocusing effects associated with Gaussian shaped structures. The precursor is not a significant phase for 5º or 10º wide Gaussian shaped ULVZs (Table 1 and Supplementary Figures 1-36). The observability of this precursory phase also depends on the location of the ULVZ on source or receiver due to the different sampling of the wavefield. Consequently, the precursor for a receiver sided 10º wide ULVZ is only detectable over ~5-6º of epicentral distance across the 2D synthetic array whereas the same source-sided ULVZ produces a precursor over a larger (>10º) epicentral distance ranges (Table 1, Supplementary Figures 1-36). The SKS precursor phase, is most detectable for source-side, flat-topped ULVZ structures more than 150 km wide. The epicentral range at which the precursor is detectable is dependent upon the location of the ULVZ with respect to the SKS wavefield as well as the shape of the ULVZ (See Supplemental Figures 1-36). On the other hand, the limited epicentral distance range that allows ULVZ precursor observation on the receiver side indicates that this phase would be difficult to identify in recorded data.

3.3. SP_dKS inception point

For the PREM model, the bifurcation of SP_dKS from SKS is noticeable in waveforms beginning at an epicentral distances of ~110º, but the inception of SP_dKS for the PREM velocity model theoretically occurs as early as ~104º [Thorne and Garnero, 2004]. The presence of an ULVZ near the theoretical inception point of this

phase generates an observable bifurcation of the SP_dKS phase at shorter epicentral distances than predicted by PREM. The distance at which this bifurcation is observable is primarily influenced by the ULVZ P-wave velocity [e.g. Rondenay and Fischer, 2003]. The models shown here indicate a similar behavior, but highlight a critical difference between source- and receiver-side ULVZ locations. For source-side ULVZs wider than ~150 km the largest observed epicentral distance shift in the bifurcation is ~5º with observable SP_dKS arrivals starting at ~104.5º. In contrast, the receiver side equivalents have a maximum shift of ~3º, but more often the bifurcation shift is not observable due to interference from secondary phases (e.g. SsP_dKS) or have a shift of less than 1º (Table 1, Supplementary Figures 1-36). Such small changes of the inception point are likely not observable in sparsely populated record sections, yet large values of the shift in bifurcation distance may indicate ULVZ presence on the source-side of the ray path.

3.4. Diffraction Length and ULVZ detectability

The length of the diffracted leg along the CMB increases with epicentral distance (Figure 5). Because the diffracted path integrates over the velocity structure along the path, only shorter paths associated with SP_dKS data less than ~120º epicentral distance show measurable travel time and waveform effects due to ULVZ interaction in recorded data (see Supplementary Material). Waveforms of SP_dKS recorded at distances larger than ~120º in general resemble PREM waveforms. To determine the sensitivity of each synthetic model for the detection of ULVZ structure along the path, while attempting to minimize the influence of the secondary phases we cross-correlate the model waveforms with those produced for the PREM base model over

374 a 20 second window centered about the SKS arrival. Figure 7 shows the results of
375 this analysis for 10º wide ULVZs with a thickness of 10 km; any correlation co-
376 efficient larger than 0.85 is considered undistinguishable from PREM. For both
377 receiver and source side ULVZs, boxcar shapes are the most detectable whereas
378 Gaussian shaped ULVZs are the least detectable based on the limited size of the
379 detectable correlation coefficient footprint (Figure 7). Detectable source side ULVZs
380 have the near edge located at no more than 15º co-latitude. Source side ULVZs are
381 also detectable over a wider range of distances (more than 5º epicentral distance)
382 whereas receiver side ULVZs are only detectable over a narrow (less than 5º)
383 epicentral distance corridor (Figure 7a,c,e). This implies that source-side ULVZs are
384 easier to detect using the SP_dKS phase. Receiver side ULVZs are most detectable for
385 ULVZs located with a near edge between 87.5º and 92.5º; the strong secondary
386 "point diffractor"-like phase discussed in the previous sections generates the key
387 correlation signals at larger distances (Figure 7b,d,f). The limited regions defined by
388 correlation coefficients in which an ULVZ is detectable using the SP_dKS system
389 further implies that imagining ULVZs requires specific source receiver geometries in
390 order to be imaged partly explaining the many non-observations in SP_dKS data. The
391 SP_dKS phases generated by ULVZ models with these specific material properties and
392 thickness outside the co-latitude limits described above would likely be
393 indistinguishable from PREM SP_dKS phases especially in the presence of noise in
394 recorded observations.
395 Consequently, this implies that it will be virtually impossible to image source side
396 ULVZs sampled only by SP_dKS with stations at distances larger than ~115º

epicentral distance. For receiver side ULVZs SP_dKS data become more complex at large epicentral distances. While SP_dKS itself behaves identically to the source side SP_dKS, the secondary phase for models with a near edge between 100º and 105º co-latitude actively interferes with SP_dKS arrivals for seismic traces between 115º and 120º epicentral distance (See Supplemental Figures). Therefore the newly observed late phases ($Ss_{top}PKS$,$Sp_{top}PKS$) might be the key to further ULVZ detections at larger distances.

One of the main observables based on these synthetics is the interaction of the SKS phase with the top of the ULVZ rather than the SP_dKS phase itself (Figure 3,6, Supplementary Figures). The interference of the energy produced by this interaction with the SP_dKS results in reduced detectability of the early bifurcation and generates strong secondary phases with a significantly different ray parameter for receiver side ULVZs (red lines in Figure 6). This indicates that ULVZs less than 600km wide have different source/receiver side characteristics and secondary phases may be applied to ascertain the sidedness of an ULVZ.

The extensive modeling of this study highlighted several unknown waveform effects allowing better characterization of ULVZ properties. Using waveform information it might be possible to identify the shape of ULVZs which is important for understanding the dynamics of ULVZs at the CMB (Bower et al., 2011). Using later arriving phases it might be possible to identify the exact location of the ULVZ along the raypath and resolve the inherent ULVZ source-receiver side ambiguity of SP_dKS.

4. ULVZs at the southern edge of the African Superplume.

The synthetic modeling presented in the previous sections indicates that the SKS/SP$_d$KS system generates a distinct fingerprint for a given ULVZ location, size and geometry. We apply these findings to a new dataset using stations in Turkey that provides us with CMB sampling in the vicinity of the northern edge of the African Large Low Shear Velocity Province (LLSVP) that has not been probed for ULVZ structure before [see summary of previous ULVZ observations in McNamara et al., 2010].

Recent large-scale deployments of seismic stations across Anatolia provide a well-suited dataset to study how the waveform behavior of finite sized ULVZs observed in the 2.5D synthetics may be applied to determine ULVZ location, elastic parameters and geometry. We use broadband data from station deployments of the Kandilli Observatory and Earthquake Research Institute Network (IRIS network code: KO), the Turkish National Network (TU), the PASSCAL North Anatolian Fault experiment (YL), and available data from European networks available via Orfeus (http://www.orfeus-eu.org) from 2005 to the middle of 2010. The resultant dataset consists of 449 individual stations comparable in size to the USArray network albeit with less regular station spacing. The combination of these networks provides a large aperture array with sufficient data coverage to analyze SKS and SP$_d$KS/SKP$_d$S waveforms generated by deep focus events in South America, the South Sandwich Islands and the West Pacific (Figure 8). This dataset, especially waveforms from

442 events in the Americas, sample the CMB in the proximity of the northern edge of the
443 African LLSVP upon exit from the core (Figure 8) [Grand, 2002; Garnero and
444 McNamara, 2008; Lekic et al. 2012] as well as CMB areas beneath South America,
445 the Caribbean, the southern Atlantic, western Pacific and western Asia. Due to
446 station locations the northern and western boundary of the African LLSVP is not
447 well sampled despite efforts from previous work using events from both the South
448 Atlantic and Africa [e.g. Helmberger et al., 2000; Ni and Helmberger, 2001; Ni and
449 Helmberger, 2003]. Many of the regions sampled in this study are either new or are
450 areas where previous work indicates a mix of ULVZ detections and non-detections
451 in individual studies, for example beneath South America .
452 In our data analysis we follow the approach presented in Thorne et al.
453 [2013b] with one key difference, for this data set we make no assumption on which
454 side of the ray path the ULVZ exists on prior to analysis. Raw data are first
455 transferred to a displacement signal using available pole-zero metadata and
456 bandpass filtered to frequencies between 0.04 Hz and 0.5 Hz. We limit our data to
457 events with earthquake depths larger than 100 km and select events with simple
458 source-time functions. Additionally, we require that there is data coverage for each
459 event between 90º and 100º epicentral distance such that a source time function
460 can be constructed and subsequently deconvolved from the time series to permit
461 combining data from multiple events. Here we are assuming that any possible
462 waveform distortion between 95º-100º will be eliminated by the stacking process.
463 This selection leads to a total usable data set of 29 events. We deconvolve the source
464 from the data by using the stacked SKS waveform for epicentral distances less than

100° as an estimate of the source wavelet and apply a water-level deconvolution with a k-value equal to 0.2 [Clayton and Wiggins, 1976]. We next grid the data into 2.5º by 2.5º geographic bins based on SP_dKS inception points (the point where P-diffraction initiates on the CMB) for all source and receiver regions containing at least one 5º by 5º square with a minimum 100 inception points (Figure 8, 9, 10). This results in four source-side regions with dense data coverage beneath: (1) South America (Figure 9a), (2) the Caribbean (Figure 9b), (3) the South Sandwich Islands (Figure 9c) and (4) the West Pacific (Figure 9d). These regions sample a wide variety of mantle environments from subduction dominated regions (Figure 9a, b) to LLSVP border regions (Figure 9c,d) [Grand, 2002]. The receiver side inception points sample: (1) the northeast corner of the African LLSVP beneath the Mediterranean (Figure 10a) and (2) what appears to be more normal mantle beneath continental Eurasia (Figure 8, 10b). As we make no a-priori assumption as to the probable location of any ULVZ, each region is analyzed individually. For each geographic bin the data are stacked in 1º epicentral distance bins and cross-correlated with approximately six-hundred 2.5D synthetic waveform models (see Table 2 for details). To account for the high frequency content of our 2.5D models, we run multiple sets of cross-correlations for each bin with the synthetic data bandpass filtered between 0.04 Hz and 0.5 Hz as well as synthetic data bandpass filtered between 0.04 Hz and 0.2 Hz. In practice, the dominant period of the observed waveforms is on the order of 5-10s.

We determine the best-fit model by finding the maximum mean cross-correlation coefficient for geographic bins containing a minimum of five 1°

epicentral distance binned waveforms and more than 15 individual waveforms (Figure 11). We run cross-correlations for the time window between 10 s before SKS to 20 s after SKS to account for the possible presence of SP_dKS for each individual binned trace before calculating standard statistics for the record section, including the mean, standard deviation, median, quartiles, minimum, and maximum correlation coefficient.

To determine if this best fit model provides a better fit than PREM, we apply multiple metrics. For each individual 2.5° × 2.5° geographic bin we first apply a cross-correlation cutoff. If the mean correlation coefficient between 1° epicentral distance data stacks and synthetics for the PREM waveforms is greater than 0.78 then the bin is classified as PREM-like. Waveform inspection indicates that PREM-like and ULVZ-like waveforms are essentially indistinguishable for mean correlation coefficients larger than 0.78. We therefore assume that if the mean correlation coefficient is less than 0.78 the geographic bin possibly contains ULVZ structure. We next compare data stacks to the synthetics generated for our suite of ULVZ models. We next determine which ULVZ model provides the best-fit (based on mean cross-correlation coefficient). If the best-fit model has a mean cross-correlation greater than PREM's mean cross-correlation plus 1 standard deviation, then we further consider the bin to be possibly ULVZ-like. Considering only simple standard deviations when comparing model fits often results in overlapping or near overlapping values. For example, the South American grid node SA_E10 (Figure 9a, 11) has 165 individual seismograms over all 17 epicentral distance bins (104º-120º). The cross-correlation results for the 0.04-0.2Hz bandpass filtered data

511 indicate that a boxcar ULVZ with a length of 10º located 5º away from the source
512 would be the best-fit model with an average cross-correlation coefficient of
513 0.76±0.10. Comparable PREM models reach cross-correlation values of 0.71±0.05.
514 The PREM model does not reach the minimum cross-correlation coefficient and the
515 ULVZ model has a higher average correlation coefficient. The ULVZ model would
516 therefore move on to the next step in analysis based on the raw numbers of the
517 mean correlation coefficient, but it is important to note that the standard deviations
518 of the two models do overlap. Given that we are examining a population with only a
519 small change in the measure of fit, correlation coefficients, a simple confidence
520 about the mean is not the best measure to compare the models. To determine the
521 quality of a fit of waveforms for PREM vs. an ULVZ model a better metric is required
522 than simple mean comparison. In this analysis we pass these type results into the
523 visual inspection process. The development of a robust statistical metric to be
524 applied in lieu of or in conjunction with the mean is a venue for future study.
525 Waveform matches for the South American grid E10 for both the PREM
526 (Figure 11b) and the best-fit ULVZ model (Figure 11c) are shown in Figure 11; the
527 most substantial mismatch is due to slight differences in the frequency content of
528 the 2D models. Critically, these data (black lines in Figure 11) do not have a clear
529 SP_dKS phase at 110º epicentral distance as required by the best-fit ULVZ model
530 (Figure 11b). Indeed, the worst fitting portion of the ULVZ model is between 109°-
531 114º epicentral distance where the sensitivity to the model ULVZ is greatest. The
532 ULVZ model, however, does better match the timing of the observed SP_dKS arrival
533 between 114-117º. A conservative interpretation would err towards a null

detection whereas a less conservative interpretation based on timing match between 114°-117º of the SP_dKS arrival would detect evidence for a ULVZ. In this case we mark the result as inconclusive/possible ULVZ; the dashed white lines in Figure 9 outline the possible ULVZ regions. It is worth noting that this particular example is an extreme borderline case between ULVZ detection and non-detection and as with any human based method open to interpretation. Here we elect to be extremely conservative only interpreting ULVZ detections if there is a clear early inception of the SP_dKS phase in the data. This minimizes the possibility of false positives, but may eliminate detections of subtle ULVZ structure.

We observe a similar situation for the Mediterranean receiver side grid node D4 (MED_D4) (Figure 10a, 11d-f). Here the PREM model has a mean correlation coefficient of 0.77±0.03 whereas the best-fit ULVZ model, a 10º long boxcar with a height of 10km, V_P reduction of 10%, V_S reduction of 30%, density increase of 10%, and left-edge location 5º from the source, has a mean cross-correlation coefficient of 0.81±0.10. As with the South American grid node SA_E10, there is significant mismatch between the observed inception point of the SP_dKS and the ULVZ model, and a better timing match of the SP_dKS arrival at larger epicentral distances between 114-118º (Figure 11d-f). Interestingly, this receiver side grid node indicates a preference for a source-side ULVZ beneath South America in the similar location as the ULVZ modeled in SA_E10 with the same properties. As with the former case for SA_E10, the more conservative interpretation of no ULVZ/possible ULVZ is preferred.

556 The data analysis method presented here has the advantage that the first
557 two numerical analysis tests, PREM correlation coefficient cutoff and mean test can
558 be performed automatically. This reduces the number of required visual inspections
559 for large datasets. However, as the example for SA_E10 and MED_D4 indicates, the
560 visual inspection is still a critical step for determining whether a confirmed ULVZ
561 model is warranted for a given dataset.
562 The data analysis in this study uses extremely stringent requirements to
563 obtain a positive identification of an ULVZ. Consequently, the majority of the results
564 do indicate PREM-like CMB structure. Due to the restricted size of our synthetic
565 model library there may be some cases where a ULVZ structure is probable, but the
566 current model library does not contain the correct parameters or the diffracted path
567 sampling is not sufficient to determine ULVZ structure. It is important to note that
568 this method is essentially a grid search of forward models; the method's
569 effectiveness is dependent upon the completeness of the library. An expanded
570 model library may be able to find an ULVZ model match for some grid nodes
571 assigned a PREM value, but given the required computation time for a single model
572 (~36-72 hours per model using eight 2GB processes on the ARC1 parallel cluster
573 based in the University of Leeds which uses Intel X5560 2.8GHz processors or eight
574 2GB processes on a single computer with 32Gb RAM and an Intel quad core
575 processor) a complete ULVZ SP_dKS waveform library with variations in ULVZ height,
576 velocity, and density requires significant time and commitment and does not seem
577 feasible at the moment.

With these strict requirements for detection we do not identify ULVZs for the South American, Caribbean, or West Pacific source-side geographic bins, but do identify one ULVZ near the South Sandwich Islands (Figure 9) which is discussed further below. All of the receiver-side geographic bins (Figure 10) do not contain a detectable ULVZ structure. This majority null result that includes some borderline cases such as the South American case (SA_E10) previously described is consistent with the mixed and null results previously recorded in these regions [Idehara et al., 2007; Persh et al., 2001; Thorne and Garnero, 2004]. We do not detect the ULVZ imaged by Zou et al. (2007) using PKP data within the South American grid. There are two potential explanations for this seemingly contradictory observation: The grid overlapping the region sampled by Zou et al. [2007] is the same region sampled by the borderline case described for the South American grid E10; the null detection could be the result of the very strict restrictions we apply to the automated detection system, the misfit with a particular ULVZ model in the library and/or a small scale ULVZ sampled by a minority of the diffracted paths. Nonetheless, our results indicate that the waveform is most likely well explained by a PREM-like CMB region.

The results using the strict cut-off and semi-automated detection do indicate that there exists an ULVZ in the South Atlantic. The grid references SSI_D2, SSI_E2, and SSI_E3 indicate that there is likely a ~3º wide boxcar shaped ULVZ approximately 13º away from the source location (Figure 12 and Supplementary Figures 37-38). Figure 12 shows the modeling results for the South Atlantic Grid E2 (SSI_E2). Here the PREM model yields cross correlation coefficient of 0.74±0.11

(Figure 12a); the best-fit boxcar ULVZ model (Figure 12b) with a near edge location of 13º and length 3º has a correlation coefficient of 0.87±0.07. Upon visual inspection the ULVZ model successfully models the inception of SP_dKS at approximately 108º epicentral distance (Figure 12b) whereas the PREM model does not match the observed inception point. The model library applied in this case study included Gaussian and trapezoid shaped ULVZs yet the best-fit model was a boxcar shaped ULVZ. The best-fit Gaussian model with a near edge location at 12.5º co-latitude and a length of 5º (~300 km) has a mean correlation coefficient of 0.84±0.07 while the best-fit trapezoid model with a near edge location at 10º co-latitude and length of 5º has a mean correlation coefficient of 0.82±0.08. While the mean correlation coefficient is not significantly different for any of the model types, the median correlation coefficients for the best-fit boxcar, Gaussian, and trapezoid models are 0.87, 0.83, and 0.82 respectively indicating that the boxcar model is a better fit for the overall dataset given the current models available in the model library.

The significance of secondary phases was discussed and observed in the earlier sections describing the synthetic results. The data here do not indicate a clear secondary phase, but the data show small arrivals about 7-10 s after the SKS specifically for distances of 104º and 108º-116º (Figure 12). While the signal is not strong enough to provide a positive identification it does indicate that searching for the secondary reflections related to SKS may be possible. Such a search, however, would require an event based analysis so that data between 90º and 104º could be effectively analyzed.

624 The identification of this ULVZ structure is of particular interest as it is
625 located less than approximately 300 km off the southern edge of the African LLSVP
626 as indicated in tomographic images (Figure 8, 9c). While the detection of ULVZ
627 structure along the border of a LLSVP is not a new phenomenon, the majority of
628 ULVZ detections are primarily in the vicinity of the Pacific LLSVP [see McNamara et
629 al. [2010] for a review]. ULVZ structure detections in the vicinity of the African
630 LLSVP are significantly rarer partially due to less data availability to probe deep
631 mantle structures. There are a few ULVZ detections further north and south of our
632 detection [Rost et al, 2006; Wen, 2002]. Additional work has detected ULVZs and
633 low velocity structures in the South Atlantic using ScS and SP_dKS data approximately
634 10º north of our sampled location but the precise location of the ULVZ detected in
635 this study has not been probed previously [Helmberger et al., 2000; Ni and
636 Helmberger, 2001; Tkalčić and Romanowicz, 2002].
637
638 **5. Conclusions**
639 Most past studies of ULVZ structure have employed 1D methods to compute
640 synthetic seismograms in order to model ULVZ seismic properties (e.g. Sun et al.,
641 2012; Avants et al., 2006; Garnero and Helmberger, 1995; Garnero and Helmberger,
642 1996; Garnero and Helmberger, 1998). Typically, an implicit assumption is made as
643 to whether the ULVZ is located at the source- or receiver-side of the SKS path. The
644 synthetic waveforms calculated in this study indicate that ULVZ structures less than
645 600 km wide create distinct waveform patterns that can be used to differentiate
646 between source- and receiver-side ULVZs. We show that a-priori information on

ULVZ location is not necessarily needed, but that such assumptions may also lead to the false identification and location of ULVZs. We have presented a case study using a preliminary method to conduct a robust search for ULVZ structures using large aperture arrays. Most of our study region seems to be ULVZ free or may contain ULVZs below the detection threshold [Rost et al., 2010] giving more evidence to the hypothesis that ULVZs are regional phenomena. We show evidence for ULVZ structure in the South Sandwich Island region at the edge of the African LLSVP. The best-fit model for this previously undetected ULVZ in the South Atlantic indicates a steep sided ULVZ about 180 km across and 10 km high with a V_S decrease of 30%, V_P decrease of 10% and density increase of 10% relative to PREM.

It is important to note that the method applied here is essentially a grid search over a library of forward models. Despite the fact that the library in this study consists of hundreds of models, a more complete library of ULVZ models including additional velocity, density, ULVZ height parameter variations is needed. A more complete and robust synthetic library would permit directed searches when comparing synthetic waveforms with observations of the SP_dKS system. Currently, depending upon the topology and computational processors available, a single model requires between ~36 and 72 hours of runtime using eight processes on the ARC1 parallel computing cluster at the University of Leeds. In order to generate a complete model space, a community effort and funding for the generation, storage, and data basing of available 2.5D models is needed.

Acknowledgements

Most figures were generated using the Generic Mapping Tools freeware package (Wessel & Smith 1998). We thank two anonymous reviewers and editor for their constructive comments which helped us to improve the paper. We thank the Kandilli Observatory and Earthquake Research Institute (UDIM), the National Seismic Array of Turkey (AFAD-DAD), ORFEUS, and IRIS for providing the data. EV and SR were funded by NERC grant NE/H022473/1.

References

Avants, M., Lay, T., and Garnero, E. J. (2006). A new probe of ULVZ S-wave velocity structure: Array stacking of ScS waveforms. Geophys. Res. Lett., 33, L07314.

Berryman, J. (2000). Seismic velocity decrement ratios for regions of partial melt in the lower mantle, Geophys. Res. Lett., 27, 421–424.

Bower, D. J., J. K. Wicks, M. Gurnis, and J. M. Jackson (2011). A geodynamic and mineral physics model of a solid-state ultralow-velocity zone. Earth. Planet. Sci. Lett. 303, 193-202, doi:10.1016/j.epsl.2010.12.035.

Brown, S.P., M.S. Thorne, L. Miyagi and S. Rost (2015). A compositional origin to ultralow-velocity zones, Geophys. Res. Lett., 42, 1039-1045.

Burke, K., and Torsvik, T. H. (2004). Derivation of large igneous provinces of the past 200 million years from long-term heterogeneities in the deep mantle. Earth Planet. Sci. Lett., 227, 531-538.

Burke, K., Steinberger, B., Torsvik, T. H., and Smethurst, M. A. (2008). Plume generation zones at the margins of large low shear velocity provinces on the core–mantle boundary. Earth Planet. Sci. Lett., 265, 49-60.

Cottaar, S., and Romanowicz, B. (2012). An unusually large ULVZ at the base of the mantle near Hawaii. Earth Planet. Sci. Lett., 355, 213-222.

Clayton, R. W., and Wiggins, R.A., 1976. Source shape estimation and deconvolution of teleseismic body waves, Geophys. J. R. Astron. Soc., 47, 151–177.

706 Dobson, D. P., & Brodholt, J. P. (2005). Subducted banded iron formations as a
707 source of ultralow-velocity zones at the core–mantle boundary. Nature, 434(7031),
708 371-374.
709
710 Dziewonski, A. M., and D. L. Anderson (1981), Preliminary reference Earth model,
711 Phys. Earth Planet. Inter., 25, 297–356.
712
713 Garnero, E. J., and D. V. Helmberger (1995), A very slow basal layer underlying large-
714 scale low-velocity anomalies in the lower mantle beneath the Pacific: Evidence from
715 core phases, Phys. Earth Planet. Inter., 91, 161–176.
716
717 Garnero, E. J., and D. V. Helmberger (1996), Seismic detection of a thin laterally
718 varies boundary layer at the base of the mantle beneath the central-Pacific, Geophys.
719 Res. Lett., 23, 977–980.
720
721 Garnero, E. J., and D. V. Helmberger (1998), Further structural constraints and
722 uncertainties of a thin laterally varying ultralow-velocity layer at the base of the
723 mantle, J. Geophys. Res., 103, 12,495–12,509.
724
725 Garnero, E. J., and A. K. McNamara (2008), Structure and dynamics of Earth's lower
726 mantle, Science, 320, 626–628, doi:10.1126/science.1148028.
727
728 Garnero, E. J., and Jeanloz, R. (2000). Fuzzy patches on the Earth's core-mantle
729 boundary?. Geophys. Res. Lett., 27, 2777-2780.
730
731 Garnero, E. J., and Vidale, J. E. (1999). ScP; a probe of ultralow velocity zones at the
732 base of the mantle. Geophys. Res. Lett., 26, 377-380.
733
734 Grand, S. P. (2002), Mantle shear-wave tomography and the fate of subducted slabs,
735 Philos. Trans. R. Soc. London A, 360, 2475–2491.
736
737 Hier-Majumder, S., & Revenaugh, J. (2010). Relationship between the viscosity and
738 topography of the ultralow-velocity zone near the core–mantle boundary. Earth and
739 Planetary Science Letters, 299(3), 382-386.
740
741 Hier-Majumder, S. (2014). Melt redistribution by pulsed compaction within
742 UltraLow Velocity Zones. Physics of the Earth and Planetary Interiors, 229, 134-143.
743
744 Helmberger, D.V., Garnero, E.J., Ding, X., 1996. Modeling two-dimensional structure
745 at the core–mantle boundary. J. Geophys. Res. 101, 13963–13972.
746 doi:10.1029/96JB00534.
747
748 Helmberger, D., Ni, S., Wen, L., and Ritsema, J. (2000). Seismic evidence for ultralow-
749 velocity zones beneath Africa and eastern Atlantic. J. Geophys. Res., 105, 23865-
750 23878.
751

752 Hernlund, J. W., and Jellinek, A. M. (2010). Dynamics and structure of a stirred
753 partially molten ultralow-velocity zone. Earth Planet. Sci. Lett., 296, 1-8.
754
755 Idehara, K. A. Yamada, and D. Zhao (2007),Seismological constraints on the ultralow
756 velocity zones in the lowermost mantle from core-reflected waves, Phys. Earth
757 Planet. Int., 165, 25–46.
758
759 Idehara, K. (2011). Structural heterogeneity of an ultra-low-velocity zone
760 beneath the Philippine Islands: implications for core–mantle chemical
761 interactions induced by massive partial melting at the bottom of the
762 mantle. Phys. Earth Planet. Inter. 184, 80–90, http://dx.doi.org/10.1016/
763 j.pepi.2010.10.014
764
765 Jahnke, G., Thorne, M. S., Cochard, A., and Igel, H. (2008). Global SH-wave
766 propagation using a parallel axisymmetric spherical finite-difference scheme:
767 application to whole mantle scattering. Geophys. J. Int., 173, 815-826.
768
769 Jahnke, G. (2009). Methods for seismic wave propagation on local and global scales
770 with finite differences (Doctoral dissertation, Ludwig-Maximilians-Universität
771 München).
772
773 Jensen, K. J., Thorne, M. S., and Rost, S. (2013). SPdKS analysis of ultralow-velocity
774 zones beneath the western Pacific. Geophys. Res. Lett., 40, 4574-4578.
775
776 Knittle, E., & Jeanloz, R. (1991). Earth's core-mantle boundary: results of
777 experiments at high pressures and temperatures. Science, 251(5000), 1438.
778
779 Labrosse, S., Hernlund, J. W., & Coltice, N. (2007). A crystallizing dense magma ocean
780 at the base of the Earth's mantle. Nature, 450(7171), 866-869.
781
782 Lekic, V., Cottaar, S., Dziewonski, A., & Romanowicz, B. (2012). Cluster analysis of
783 global lower mantle tomography: A new class of structure and implications for
784 chemical heterogeneity. Earth and Planetary Science Letters, 357, 68-77.
785
786 Li, M., McNamara, A., and Garnero E. (2013), Three dimensional morphology and
787 dynamics of ultra low velocity zones. Fall AGU Meeting. Abstract: DI51A-2264.
788
789 Mao, W. L., Mao, H. K., Sturhahn, W., Zhao, J., Prakapenka, V. B., Meng, Y., ... & Hemley,
790 R. J. (2006). Iron-rich post-perovskite and the origin of ultralow-velocity zones.
791 Science, 312(5773), 564-565.
792
793 McNamara, Allen K. , Garnero, Edward J. and Rost, Sebastian (2010). Tracking deep
794 mantle reservoirs with ultra-low velocity zones, Earth Planet. Sci. Lett., 299, 1-9.
795
796 Müller, G. (1985), The reflectivity method: a tutorial. J. Geophys., (58): 153–174.
797

798 Ni, S.D, V. F. Cormier, and D. V Helmberger. (2003). A comparison of synthetic
799 seismograms for 2D structures: Semianalytical versus numerical. Bull. Seismol. Soc.
800 Am. doi:10.1785/0120030011.
801
802 Ni, S., and Helmberger, D. V. (2001). Horizontal transition from fast to slow
803 structures at the core–mantle boundary; South Atlantic. Earth Planet. Sci. Lett., 187,
804 301-310.
805
806 Ni, S., and Helmberger, D. V. (2003). Ridge-like lower mantle structure beneath
807 South Africa. J. Geophys. Res., 108, 2094.
808
809 Nomura, R., Ozawa, H., Tateno, S., Hirose, K., Hernlund, J., Muto, S. and Hiraoka, N.
810 (2011). Spin crossover and iron-rich silicate melt in the Earth's deep mantle. Nature,
811 473, 199-202.
812
813 Persh, S. E., Vidale, J. E., and Earle, P. S. (2001). Absence of Short-Period ULVZ
814 Precursors to PcP and ScP from two Regions of the CMB. Geophys. Res. Lett., 28,
815 387-390.
816
817 Revenaugh, and R. Meyer (1997), Seismic evidence of partial melt within a possible
818 ubiquitous low-velocity layer at the base of the mantle, Science 277,670-673.
819
820 Rondenay, Stéphane, Cormier, Vernon F., and Van Ark, Emily M. (2010), SKS and
821 SPdKS sensitivity to two-dimensional ultralow-velocity zones, J. Geophys. Res., 115,
822 2156-2202. DOI:10.1029/2009JB006733.
823
824 Rondenay, S., and Fischer, K. M. (2003). Constraints on localized core-mantle
825 boundary structure from multichannel, broadband SKS coda analysis. J. Geophys.
826 Res., 108, 2537.
827
828 Rost, S., and Revenaugh, J. (2003). Small-scale ultralow-velocity zone structure
829 imaged by ScP. J. Geophys. Res., 108, 2056.
830
831 Rost, S., E.J. Garnero, Q. Williams, and M. Manga (2005), Seismological constraints on
832 a possible plume root at the core–mantle boundary, Nature, 435, 666–669
833
834 Rost, S., E. J. Garnero, and Q. Williams (2006), Fine-scale ultralow-velocity zone
835 structure from high-frequency seismic array data, J. Geophys. Res., 111, B09310,
836 doi:10.1029/2005JB004088.
837
838 Rost, S., E. J. Garnero, and W. Stefan (2010), Thin and intermittent ultralow-velocity
839 zones, J. Geophys. Res., 115, B06312, doi:10.1029/2009JB006981.
840
841 Sun, D., Helmberger, D. V., Jackson, J. M., Clayton, R. W., and Bower, D. J. (2012).
842 Rolling hills on the core–mantle boundary. Earth Planet. Sci. Lett., 361, 333-342.
843

844 Tan, E., Gurnis, M., and Han, L., (2002). Slabs in the lower mantle and their
845 modulation of plume formation. Geochem. Geophys. Geosyst., 3, 1067.
846 doi:10.1029/2001GC000238.
847
848 Thorne, M. S., and E. J. Garnero (2004), Inferences on ultralow-velocity zone
849 structure from a global analysis of SPdKS waves, J. Geophys. Res., 109, B08301,
850 doi:10.1029/2004JB003010.
851
852 Thorne, M. S., Lay, T., Garnero, E. J., Jahnke, G., and Igel, H. (2007). Seismic imaging of
853 the laterally varying D ″region beneath the Cocos Plate. Geophysical Journal
854 International, 170, 635-648.
855
856 Thorne, M. S., Garnero, E. J., Jahnke, G., Igel, H., and McNamara, A. K. (2013a). Mega
857 ultra low velocity zone and mantle flow. Earth Planet. Sci. Lett., 364, 59-67.
858
859 Thorne, M. S., Zhang, Y., and Ritsema, J. (2013b). Evaluation of 1-D and 3-D seismic
860 models of the Pacific lower mantle with S, SKS, and SKKS traveltimes and
861 amplitudes. J. Geophys. Res, 118, doi: 10.1002/jgrb.50054,.
862
863 Tkalčić, H., and Romanowicz, B. (2002). Short scale heterogeneity in the lowermost
864 mantle: insights from PcP-P and ScS-S data. Earth Planet. Sci. Lett., 201, 57-68.
865
866 Wen, L., and D. V. Helmberger (1998), A two-dimensional P-SV hybrid method and
867 its application to modeling localized structures near the core-mantle boundary, J.
868 Geophys. Res., 103, 17,901–17,918.
869
870 Wen, L. (2002). An SH hybrid method and shear velocity structures in the
871 lowermost mantle beneath the central Pacific and South Atlantic Oceans. Journal of
872 Geophysical Research: Solid Earth (1978–2012), 107(B3), ESE-4.
873
874 Wessel P., Smith W.H.F., (1998). New, improved version of the Generic Mapping
875 Tools released, EOS, Trans. Am. geophys. Un., 79, 579.
876
877 Wicks, J. K., J. M. Jackson, and W. Sturhahn (2010). Very low sound velocities in iron-
878 rich (Mg,Fe)O: Implications for the core-mantle boundary region. Geophys Res. Lett.
879 37, L15304, doi:10.1029/2010GL043689.
880
881 Williams, Q and E.J. Garnero (1996), Seismic evidence for partial melt at the base of
882 Earth's mantle, Science 273, 1528-1530.
883
884 Zhang Y, Ritsema J, and Thorne M, (2009), Modeling the ratios of SKKS and SKS
885 amplitudes with ultra-low velocity zones at the core-mantle boundary, Geophys.
886 Res. Lett., 36, L19303, 10.1029/2009GL040030.
887
888 Zou, Z. H., Leyton, F.,and Koper, K. D., 2007. Partial melt in the lowermost mantle near
889 the base of a plume, Geophys. J. Int., *168*, 809-817.

Figure Captions

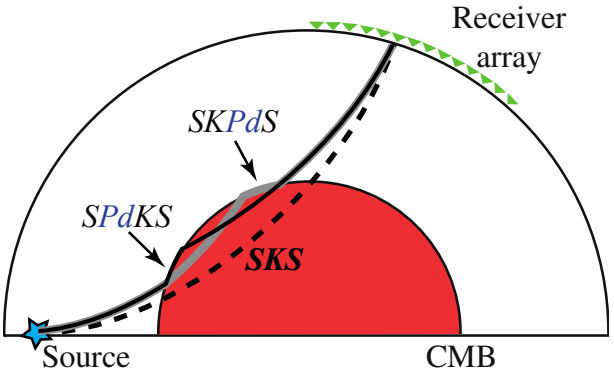

Figure 1: Schematic diagram of the SKS (black dashed line) and SP_dKS/SKP_dS (gray lines) ray paths. Note that the diffracted path of the SP_dKS/SKP_dS can occur on either the source or receiver side.

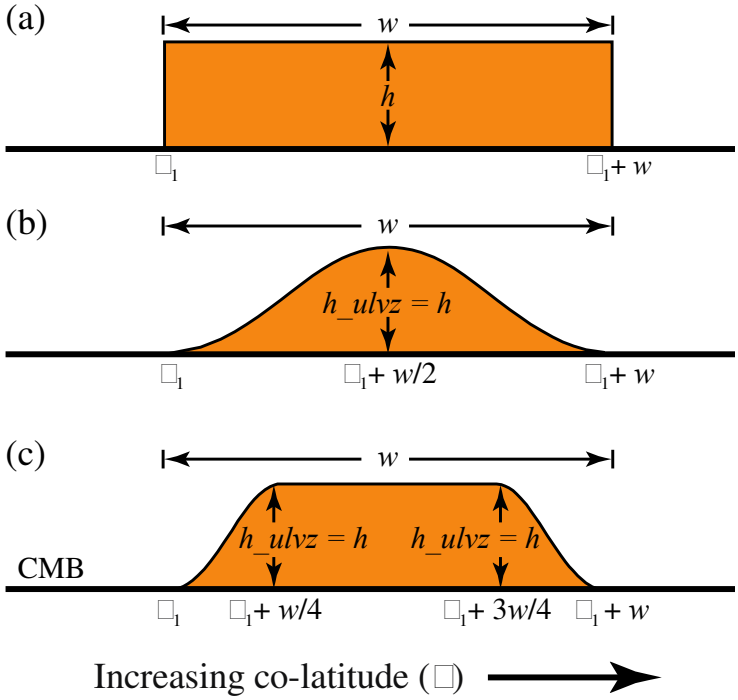

Figure 2: Schematic of the ULVZ models types, boxcar (a), Gaussian (b), and trapezoid (c) used in this study in terms of co-latitude (ø), ULVZ width (*W*), and ULVZ maximum height (*h*).

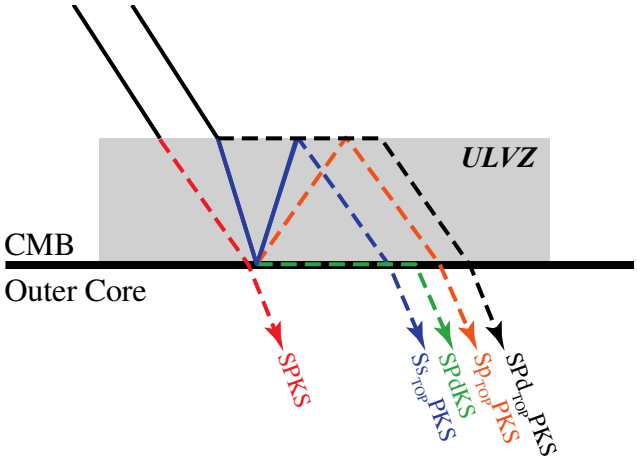

Figure 3: Schematic of phases that can be generated by an ULVZ including SP$_d$KS (green), the precursory phase SPKS (red), a diffraction along the top of the ULVZ SPd$_{top}$PKS (black), and the internally reflected phases Ss$_{top}$PKS and Sp$_{top}$PKS (blue and orange respectively).

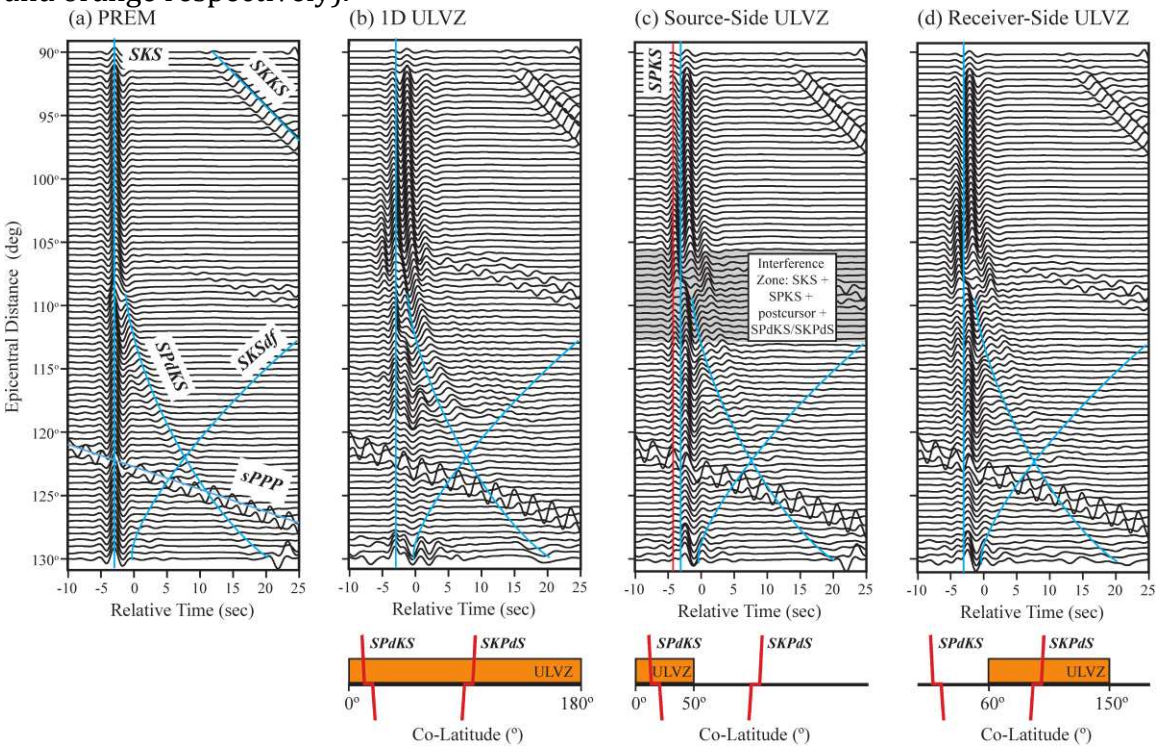

Figure 4: 2.5D base models produced by PSVaxi for the smoothed PREM model (a), a 1D ULVZ covering the whole CMB (b), a large source sided ULVZ (c), and a large receiver sided ULVZ (d). The schematics below (b), (c) and (d) denote the ULVZ structure used to generate the waveforms. Significant structures are labeled including the SKS precursor, and the SP$_d$KS/SKP$_d$S phases. Note that the waveforms in (c) and (d) are essentially identical. The red line in 4c denotes the arrival of the SPKS precursory phase. Note that waveforms and beyond 120º are dominated by the sPPP phase labeled in (a); SKS and SP$_d$KS analysis beyond this distance is

therefore not considered. A 1D ULVZ model calculated using the reflectivity code *psquik* (after Müller, 1985) with the same ULVZ parameters is shown in the supplementary material (Supplementary Figure 41)

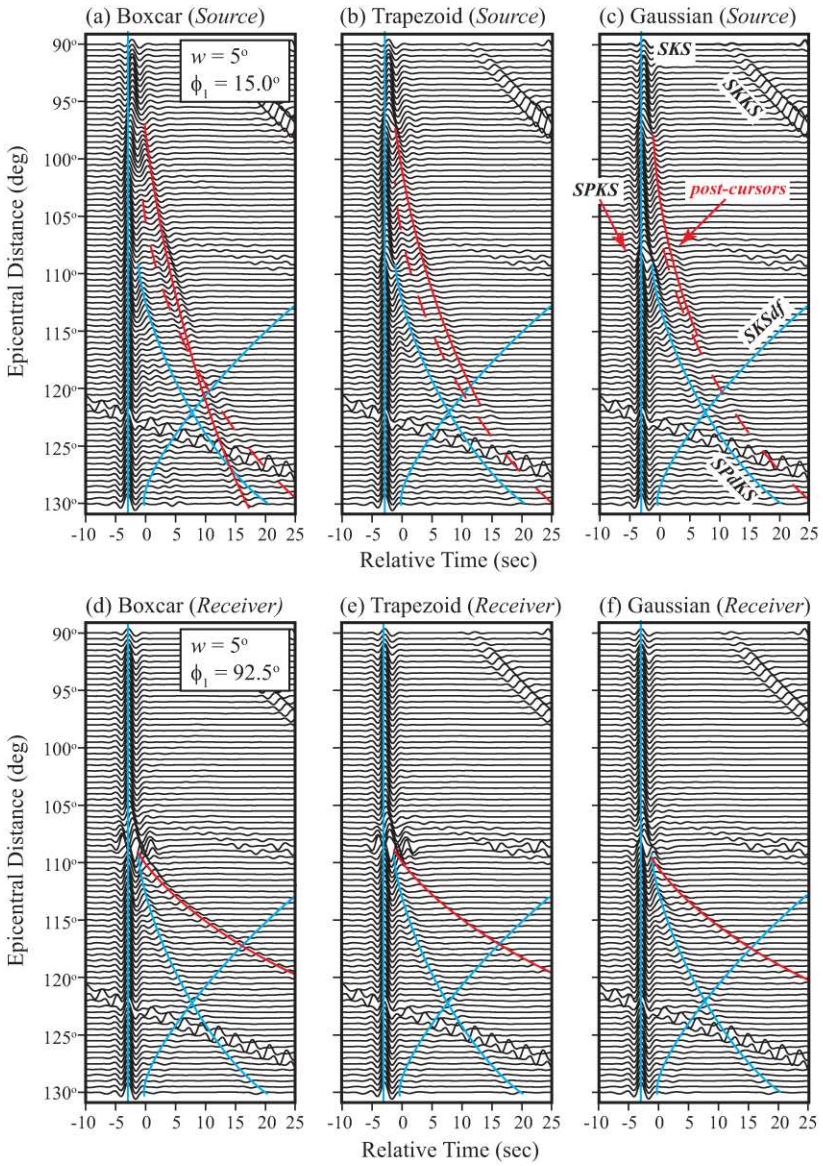

Figure 5: A selection of waveform results for a 5º long ULVZ on the source side with a co-latitude location L1=15º (top) and receiver side with L1=92.5º (bottom) for the three different types of ULVZs, boxcar (a, d), trapezoid (b, e), and Gaussian (c, f). Based on the geometry on the SP_dKS raypath the top and bottom rows are expected to be identical, but these synthetics show stark differences most notably the different inception point and ray parameter for the SKS coda phase as described in the text.

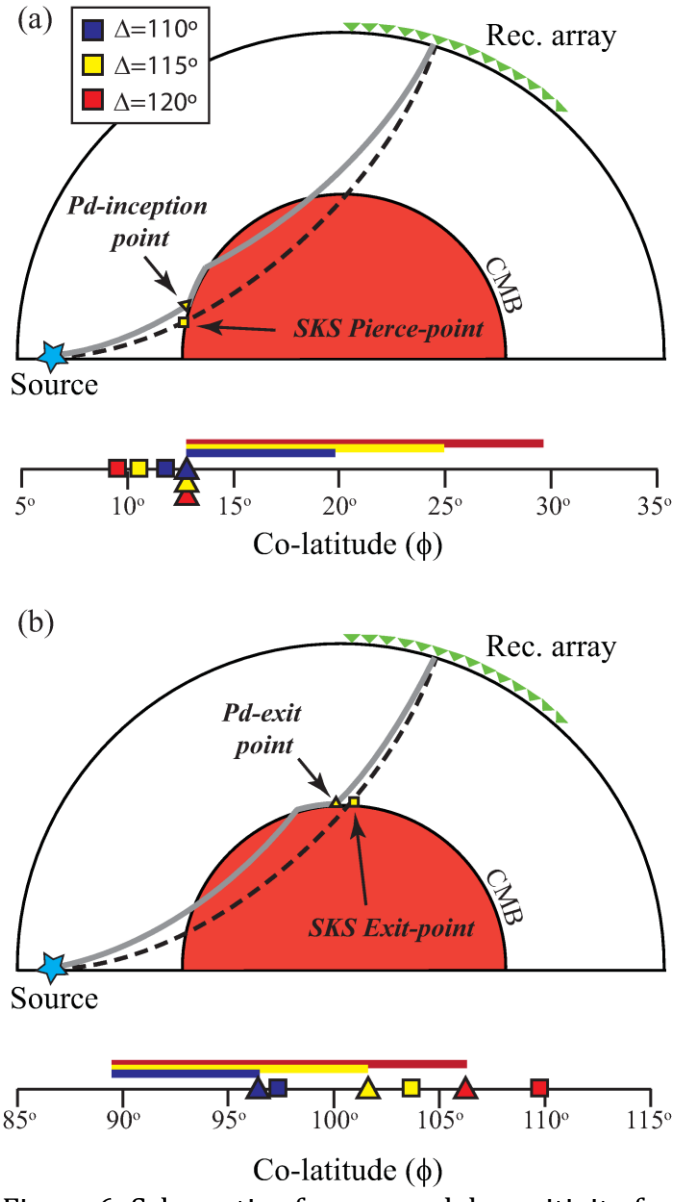

Figure 6: Schematic of array model sensitivity for the SKS and SP_dKS/SKP_dS phases for an ULVZ on the source (a) and receiver (b) side. Solid lines below the raypaths represent the coverage of the diffracted path of the SP_dKS/SKP_dS ray paths for epicentral distances of 110º(blue), 115º(yellow), and 120º(red). Triangles and squares represent the separation distance of SKS and SP_dKS/SKP_dS at the CMB and the piercing point of SKS at the CMB, respectively. Note that the major sensitivity differences between the source and receiver side stem from the piercing points of the SKS phase rather than the SP_dKS/SKP_dS paths.

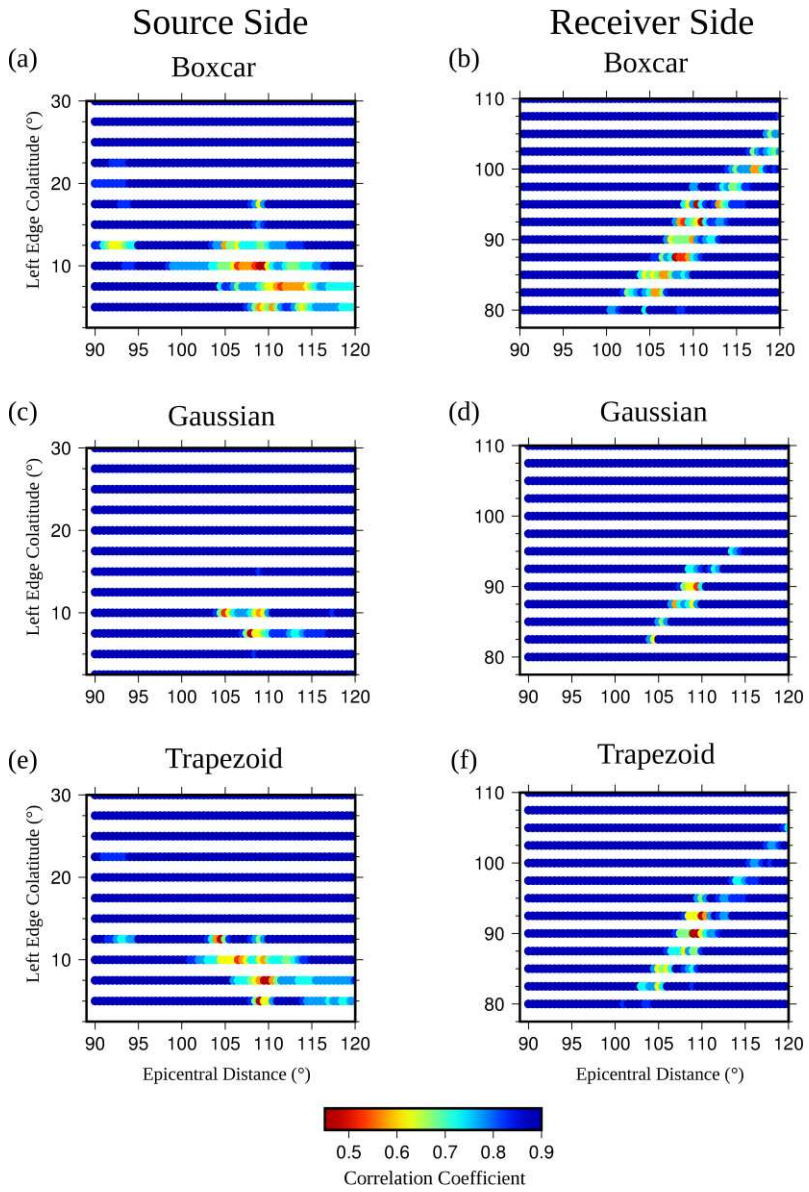

Figure 7: Results from the cross-correlation between the seismograms produced by ULVZ models and the PREM model. The plots show the resultant correlation coefficients for 10º wide ULVZs located on the source side (a, c, e) and receiver side (b, d, f) for each ULVZ shape modeled in this study, boxcar (a, b), Gaussian (c, d), and Trapezoid (e, f). The dark blue regions indicate where the correlation coefficient between the ULVZ synthetic seismograms and the PREM synthetic seismograms is greater than or equal to 0.85. The regions with high correlation coefficients are geometries where PREM and the ULVZ model would be indiscernible with the addition of noise.

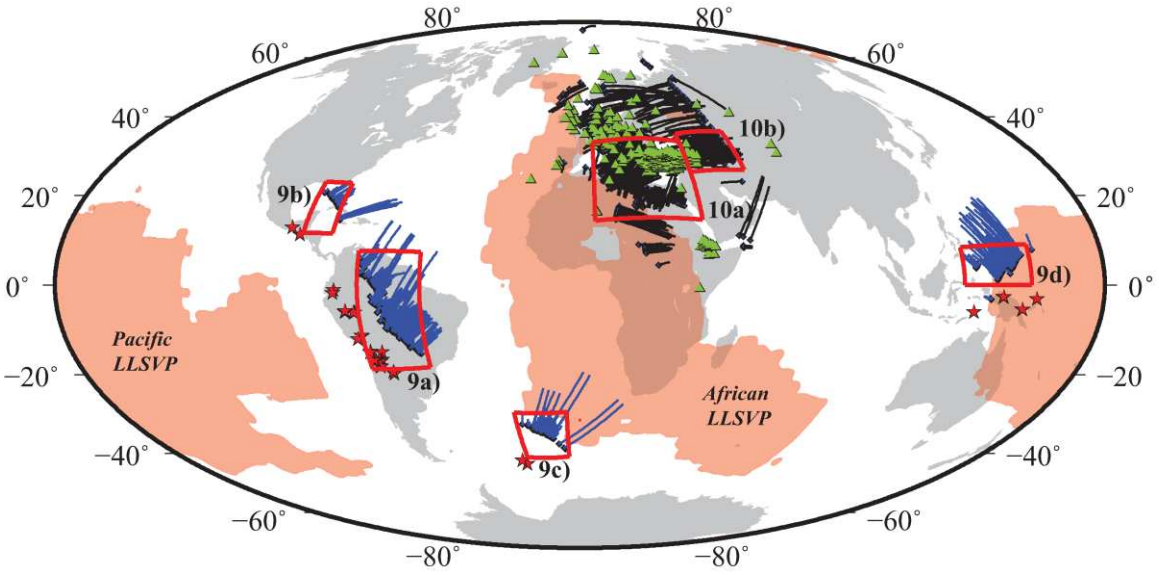

Figure 8: (a) Global station (triangles) and event (stars) distribution for the data analyzed in the case study. The outline of the LLSVPs as indicated by the -1% Vs contour of the tomographic model by Grand (2002) is shown as orange. All SP_dKS/SKP_dS diffraction paths available for analysis using the stations and events are also shown. Receiver side diffraction paths are shown in black; source side paths are shown in blue. Boxes indicate areas shown in Figures 9 and 10.

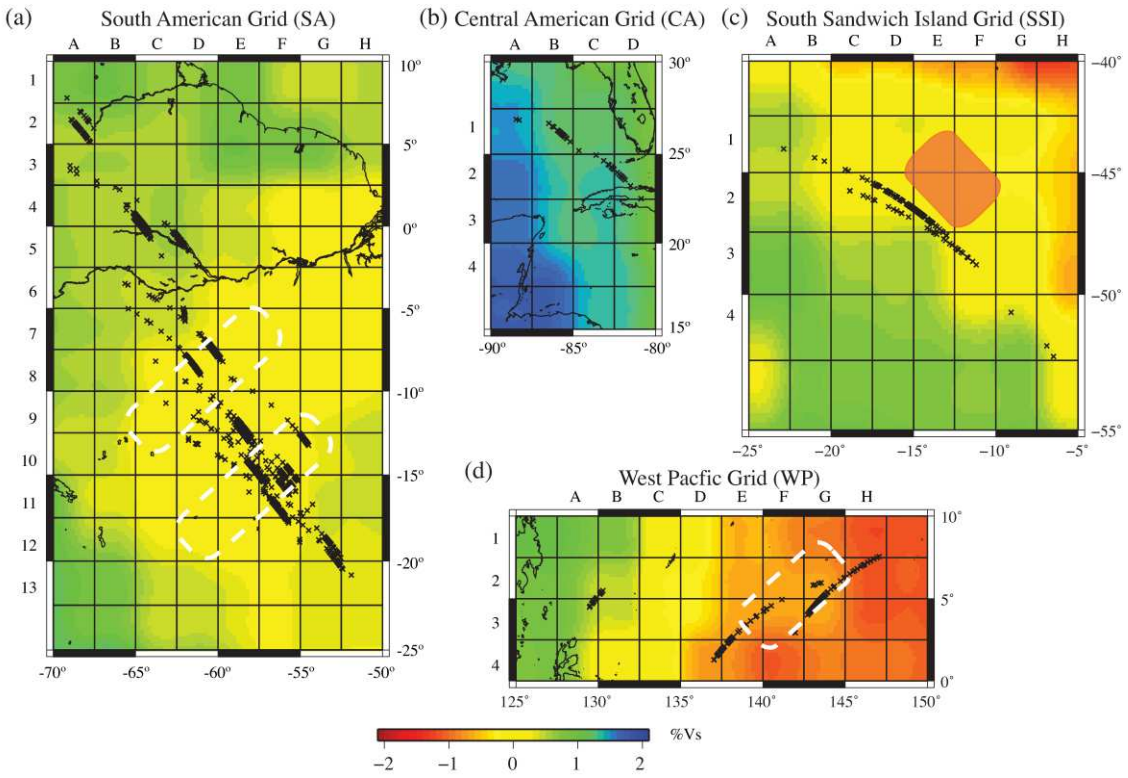

Figure 9: Source side grids analyzed in the case study underlain by the S-wave velocity perturbations at the CMB (Grand, 2002) the SP_dKS inception points are plotted as crosses. The grid labels are shown along the north and western margins for (a) the South American grid, (b) the Caribbean Grid, (c) the South Sandwich Island Grid, and (d) the West Pacific Grid. The ULVZ identified in the case study is shown in (c) by the red polygon. The white dashed lines indicate the extent of other possible but not confirmed ULVZs detected in the case study. Locations of areas are indicated in Figure 8.

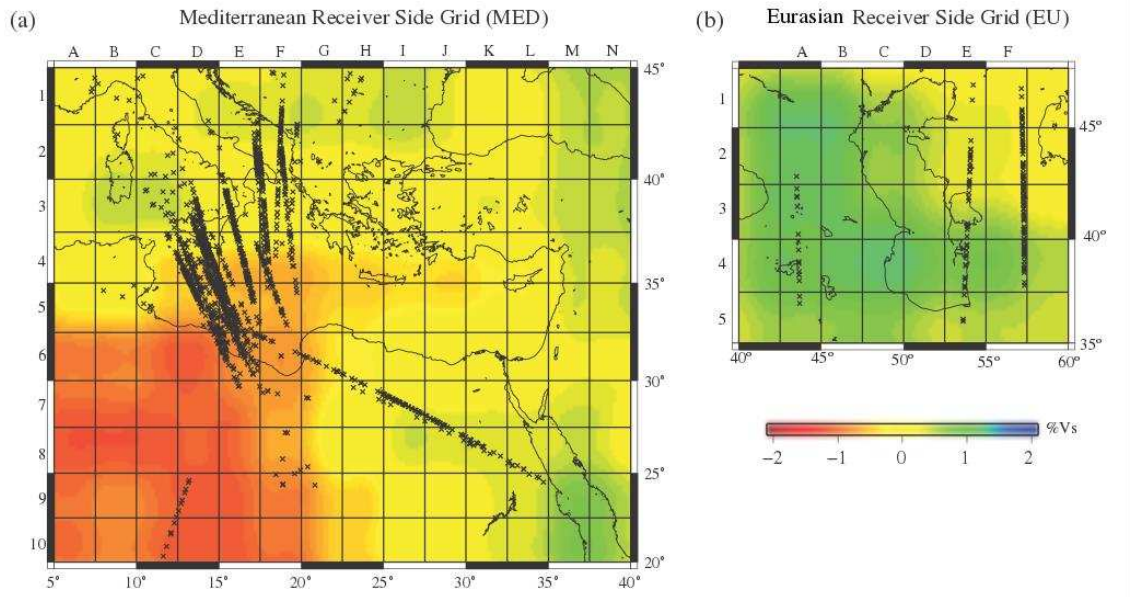

974
975 Figure 10: Same as Figure 9 but showing the receiver side grids for (a) the
976 Mediterranean and (b) the continental Eurasian grid. Locations of areas are
977 indicated in Figure 8.

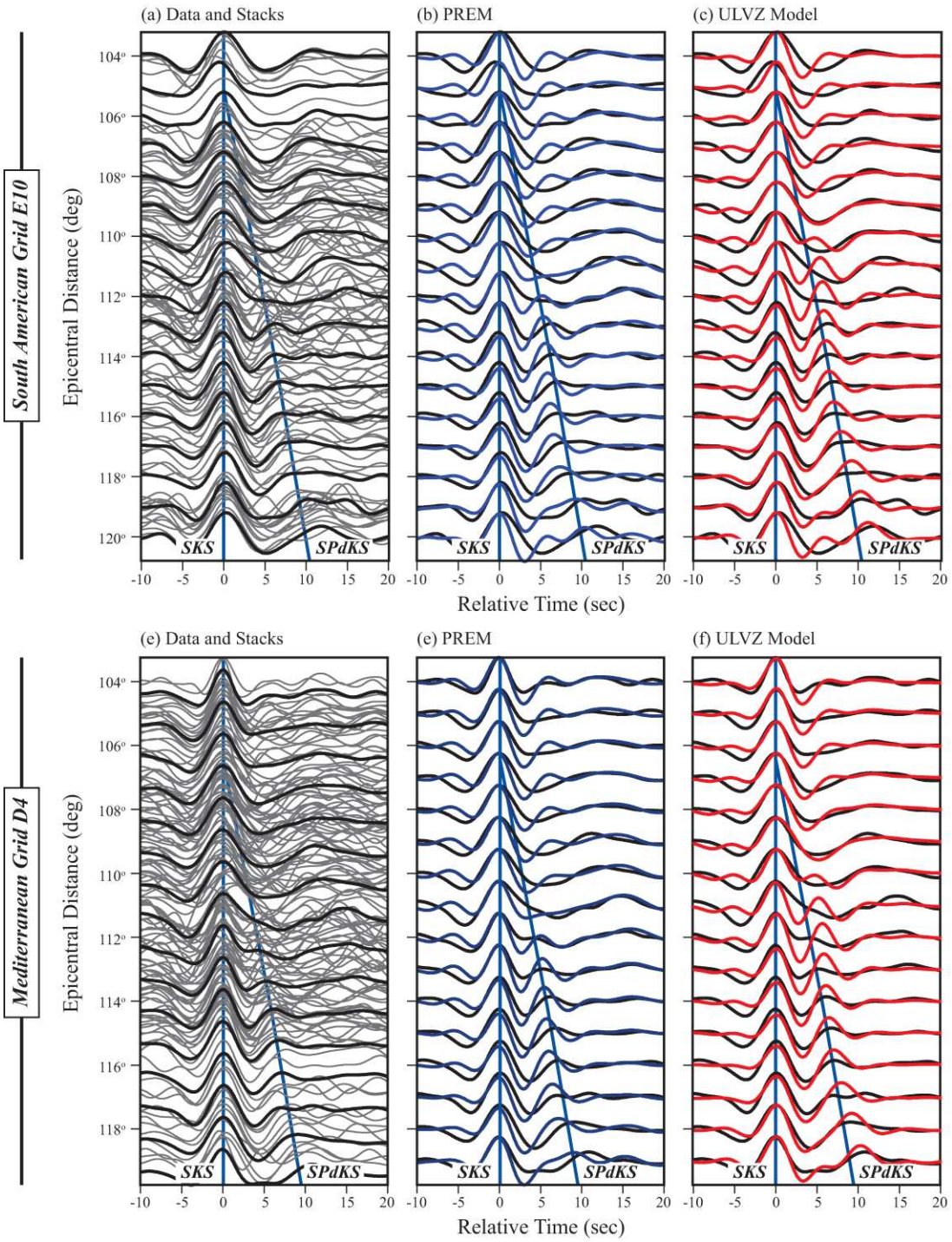

Figure 11: Example of waveforms for the South American grid node SA_E10 (a-c) and the Mediterranean grid node MED_D4. The data (black) are shown with synthetic results for the PREM model (b/e, blue), the best fit ULVZ model (c/f, red), boxcar model with ULVZ location (source side) L1=5º and length W=10º, and the raw data (a/d). Synthetics are bandpass filtered between 0.04-0.2Hz. Most of the mismatch between the waveforms can be explained by slightly differing frequency contents between the synthetic and observed data due to the source deconvolution process and subsequent stacking or attenuation of the data SKS waveform.

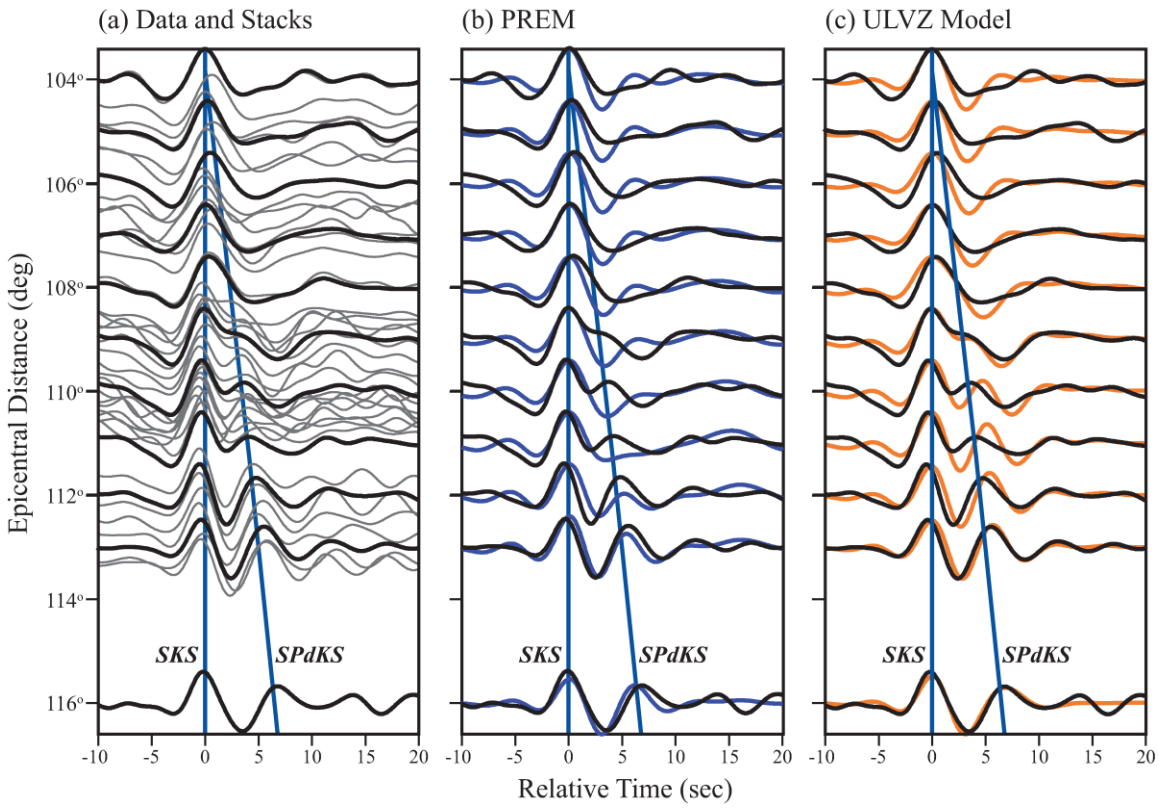

Figure 12: Example of an ULVZ detection for the South Sandwich Island grid node E2. The data (black) and stacks are shown in (a). (b) Datastacks (black) and synthetic results for PREM (blue) and (c) datastacks (black) and the best fit ULVZ model (orange). Synthetics were calculated for a boxcar model with ULVZ location (source side) L1=13º and length W=3º. The data includes a clear inception of SP_dKS near 108º epicentral distance.

Table 1: General characteristics of the synthetic 2D ULVZ models. "XX" indicates where the SP_dKS inception distance shift is not observable or is masked by interfering phases.

Shape	Length (º)	SRC/REC Side	Max SP_dKS Inception Distance Shift (º)	SKS Precursor Observed? Y/N
Gauss	2.5°	SRC	1.5°	N
Trapezoid	2.5°	SRC	0.5°	N
Boxcar	2.5°	SRC	XX	N
Gauss	5°	SRC	5°	N
Trapezoid	5°	SRC	0.5°	Y
Boxcar	5°	SRC	5°	Y
Gauss	10°	SRC	4°	Y
Trapezoid	10°	SRC	5°	Y
Boxcar	10°	SRC	6°	Y
Gauss	2.5°	REC	0.5°	Y
Trapezoid	2.5°	REC	XX	N
Boxcar	2.5°	REC	XX	N
Gauss	5°	REC	1°	N
Trapezoid	5°	REC	0.5°	Y
Boxcar	5°	REC	XX	Y
Gauss	10°	REC	XX	Y
Trapezoid	10°	REC	XX	Y
Boxcar	10°	REC	3°	Y

Table 2: SP_dKS waveform library parameter space used in the pilot case study. The V_p, V_s, and density values are set to -10%, -30%, +10% relative to the PREM model of Dziewonski and Anderson (1981) respectively. The left-edge interval is 2.5º unless otherwise stated.

Length (º)	Shape	ULVZ Height (km)	Near edge Range Co-latitude (º)
1.25	Boxcar, Gaussian, Trapezoid	10	5-30
2.5	Boxcar, Gaussian, Trapezoid	10	5-30, 75-110
3	Boxcar	10	5-21 (1º interval)
5	Boxcar, Gaussian, Trapezoid	10	5-30, 75-110
7.5	Boxcar, Gaussian, Trapezoid	10	5-30, 75-110
10	Boxcar, Gaussian, Trapezoid	10	5-30, 75-110
180 (1D ULVZ)	N/A	10	0
>40 (sided ULVZ)	N/A	10	0, 60
0 (PREM)	N/A	N/A	N/A